Continent and Life Evolution

OPEN ACCESS
Article

# Mineral chemistry and petrogenesis of chromitites from the Kangqiong ophiolite in the Bangong-Nujiang Suture Zone, Tibetan Plateau

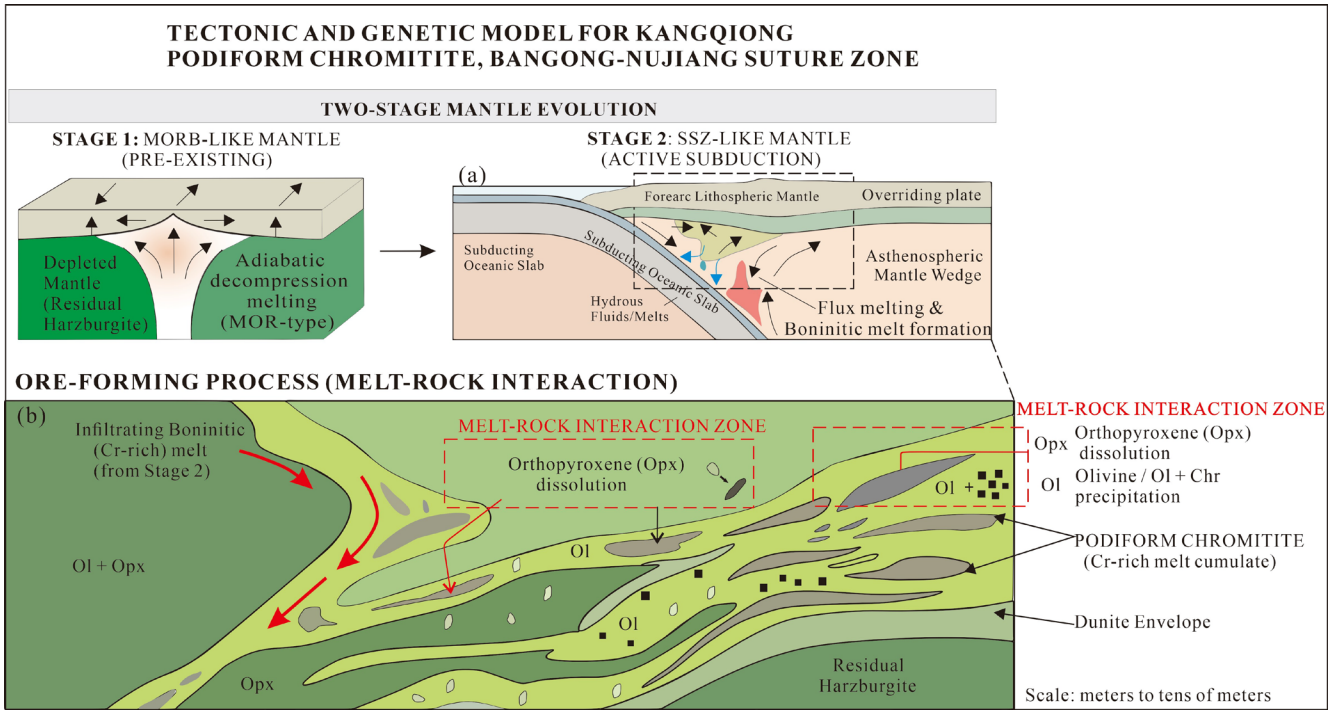
Xiaohu Lian, Ming Wang*, Quewang Danzeng, Jinlu Zhou, Binxuan Hao, Yuhe Zhang, Xin Rao and Zhenglong Li

***E-mail:** wming@jlu.edu.cn

Received 26 August 2026; Revised 17 October 2026; Accepted 18 November 2026; Published 26 November 2026

https://doi.org/10.55092/cle20260015

## Graphical Abstract




## Highlights:

- The Kangqiong chromitites show a possible boninitic affinity and may have formed through melt-rock interaction.
- Mantle peridotites record both depleted and fluid-metasomatized signatures.
- A two-stage model explains tectonic transition from MOR to subduction initiation.

Copyright©2026 by the authors. Published by ELSP. This work is licensed under Creative Commons Attribution 4.0 International License, which permits unrestricted use, distribution, and reproduction in any medium provided the original work is properly cited.

# Mineral chemistry and petrogenesis of chromitites from the Kangqiong ophiolite in the Bangong-Nujiang Suture Zone, Tibetan Plateau

Xiaohu Lian[1], Ming Wang[1,2,*], Quewang Danzeng[1], Jinlu Zhou[3], Binxuan Hao[1], Yuhe Zhang[1], Xin Rao[4] and Zhenglong Li[1]

[1] College of Earth Sciences, Jilin University, Changchun, China

[2] Key Laboratory of Northeast Asia Mineral Resources Evaluation, Ministry of Natural Resources, Changchun, China

[3] College of Construction Engineering, Jilin University, Changchun, China

[4] State Key Laboratory of Continental Evolution and Early Life, Shaanxi Key Laboratory of Early Life and Environments, Department of Geology, Northwest University, Xi'an, China

*E-mail: wming@jlu.edu.cn.

**Abstract:** Chromitites hold profound geological significance for reconstructing the evolutionary trajectories of paleo-oceanic lithospheres and the mechanical processes underlying subduction initiation. The Kangqiong chromitite deposit is geographically situated in the central-western segment of the Bangong-Nujiang Suture Zone (BNSZ) on the Tibetan Plateau, primarily hosted within highly depleted metamorphic peridotites characteristic of a typical ophiolitic accretionary mélange. Through field geological observations, high-precision mineral chemistry analyses and comprehensive whole-rock major and trace element geochemical testing, the present study systematically elucidates the genetic mechanisms of this chromite and evaluates its broader tectonic implications within the framework of continental and oceanic evolution. The analytical results indicate that the Kangqiong chromitites have $Cr^{\#}$ values of 65.06–66.58 and exhibit low titanium dioxide content ($TiO_2$ < 0.3 wt.%).The surrounding host metamorphic peridotites possess variable $Mg^{\#}$ values and are profoundly depleted in highly fusible magmatophile components such as $Al_2O_3$ and $TiO_2$. Some peridotite samples also show variable concentrations of fluid-mobile elements, but these data may have been affected by post-magmatic alteration. Together with the depleted HFSE and REE patterns, these features are compatible with a possible tectonic transition from a mid-ocean ridge (MOR) setting to a forearc supra-subduction zone (SSZ) environment, although the source and timing of the fluid-related modification remain uncertain. Accordingly, we propose a two-stage metallogenic evolution model: an early stage of decompression melting at a mid-ocean ridge that generated the foundational depleted harzburgite, followed by a possible subduction-initiation stage involving fluid-assisted melting and the generation of melts with a possible boninitic affinity.

**Keywords:** Bangong-Nujiang Suture Zone; Kangqiong ophiolite; chromite; mineral chemistry; subduction initiation; melt-rock interaction

## 1. Introduction

Podiform chromitites, predominantly hosted in the mantle peridotites of ophiolite sequences, are crucial petrological probes for understanding the evolution of the oceanic lithosphere and deep-seated magmatic processes (Leblanc and Nicolas 1992; Yuan *et al.* 2025). The formation mechanism of podiform chromitites is highly complex and has long been a subject of intense debate within the geological community (Zhang *et al.* 2017).

In recent years, the "melt-rock interaction" theory has gradually emerged as the prevailing framework for explaining their genesis. This theory posits that chromitite enrichment is not merely the result of direct crystallization from magma, but rather arises when a deep unsaturated melt migrates upward through the mantle lithosphere, undergoing intense physicochemical reactions with the surrounding mantle peridotites. These reactions induce abrupt compositional changes in the local system, thereby triggering the oversaturated precipitation of chromian spinels (Zhang *et al.* 2017; Yang *et al.* 2022a; Ma and Yang 2025; Xiong *et al.* 2026). Furthermore, the associated anomalous minerals and inclusions within podiform chromitites provide rich geochemical insights into

mantle evolution and deep-seated metallogenic processes (Bai *et al.* 2004; Xiong *et al.* 2022, 2025).

Extensive mineralogical data indicate that the composition of chromian spinels (particularly the $Cr^{\#}$ value [Cr/(Cr+Al) * 100]) exhibits high sensitivity to the properties of the original parental magma and its tectonic setting (Zhou *et al.* 2014). Chromian spinel compositions provide useful, although not unique, constraints on the nature of their parental melts and tectonic setting. Low- to medium-Cr compositions ($Cr^{\#}$ < 65) are commonly associated with mid-ocean ridge basaltic (MORB) or back-arc basin magmatic systems (Arai 1994; Zhou *et al.* 1996), whereas $Cr^{\#}$ values above 70 are more typical of chromitites crystallized from boninitic melts in supra-subduction zone (SSZ), particularly forearc, environ-ments. The Kangqiong chromian spinels have $Cr^{\#}$ values of 65.06–66.58, falling within an intermediate range between these compositional fields. Their $Cr^{\#}$ values alone therefore do not uniquely demonstrate a boninitic origin; however, when considered together with their low $TiO_2$ contents, calculated $Fe^{3+}/\Sigma Fe$ ratios, and geological context, they are compatible with a possible SSZ-related parental melt affinity (Zhou *et al.* 2014; Zhang *et al.* 2024a). Therefore, the mineral chemistry and petrogenesis of these chromitites provide vital archives of fluid-fluxed melting and forearc mantle dynamics during subduc-tion initiation.

The Bangong-Nujiang Suture Zone (BNSZ) in the central Tibetan Plateau represents the remnants of the Meso-Tethys Ocean and hosts numerous dismembered ophiolitic fragments. Ophiolites within this zone (e.g., Dongqiao, Amdo, and Dingqing), preserve records of regional ophiolite evolution and are particularly useful for understanding the geodynamic transition from mid-ocean-ridge (MOR) spreading to intra-oceanic subduction (Liu *et al.* 2020; Xie *et al.* 2025; Li *et al.* 2026). The Kangqiong ophiolite, located in the central-western segment of the BNSZ, preserves a relatively well-exposed mantle sequence, serving as an ideal natural laboratory to investigate these mantle processes. Previous studies have identified Early Cretaceous (~115 Ma) boninitic dikes within its crustal sequence, strongly suggesting a forearc SSZ setting triggered by subduction initiation (Xu *et al.* 2015). However, the deep-seated mantle response during this critical tectonic transition, particularly the genesis of the mantle-hosted podiform chromitites and their exact petrogenetic relationship with the forearc magmatism, remains enigmatic. To address this issue, we present detailed petrological, mineralogical, and whole-rock geochemical data for the podiform chromitites and their host peridotites from the Kangqiong ophiolite. By characterizing the mineral chemistry and host-rock geochemistry and field observations, this study aims to: (1) robustly constrain the parental magma affinity of the chromitites; (2) elucidate the melt-rock interaction and refertilization processes in the upper mantle; and (3) explore a possible two-stage metallogenic evolution model within the context of the tectonic transition from MOR to SSZ, thereby providing a microscopic minera-logical reference for evaluating podiform chromitite formation.

## 2. Geological setting

### *2.1. Regional geology of the Bangong-Nujiang Suture Zone*

The Bangong-Nujiang Suture Zone acts as the definitive, primary tectonic nexus bridging the Lhasa block to the south and the Qiangtang block to the north, situated deep within the central heartland of the Tibetan Plateau. This suture zone comprehensively preserves the complete tectonic lifecycle—from initial rift opening and steady-state mid-ocean ridge (MOR) expansion to terminal subduction and final collision of the Meso-Tethys ophiolitic sequences. The macroarchi-tecture of the BNSZ is geographically dominated by the widespread, discontinuous exposure of ophiolitic mélange belts, which represent the highly deformed, sheared, and obducted fragments of the paleo-oceanic lithosphere (Wang *et al.* 1987; Liu *et al.* 2020; Li *et al.* 2026; Liu *et al.* 2026). These fragmented lithospheric belts are intimately interleaved with exceedingly thick, highly deformed sequences of Jurassic to Cretaceous marine flysch deposits, which are predominantly characterized across the region as the Mugagangri Group (Figure 1). The Mugagangri Group is a critical research target for understanding the subduction and accretion history of the Meso-Tethys Ocean, as it fundamentally represents an immense accretionary wedge complex built along the active continental margin. These extensive sedimentary records supply crucial stratigraphic evidence for tracing the provenance pathways, the sedimentological infilling of the shrinking ocean basin, and the protracted structural evolution of the ancient ocean (Li *et al.* 2017).

Multiple podiform chromitites deposits of varying scale have been identified within the serpentinite bodies—Dongqiao, Yila Mountain, Amdo, and Dingqing—in the Central–Eastern segment of the BNSZ. For example, the widespread occurrence of Cr chromite deposits in the Dingqing and Dongqiao serpentinites, which are controlled by subduction-related processes, documents a complex history of melt–rock interactions (Wang *et al.* 2016; Liu *et al.* 2020; Li *et al.* 2024). However, compared to the abundant exploration achievements in the Central–Eastern segment, the oceanic lithospheric characteristics and chromite mineralization potential of the Central–Western segment of the BNSZ have not been systema-tically elucidated for an extended period due to the

influence of complex post-tectonic thrusting events (Li *et al.* 2019; Cao *et al.* 2022; Zhang B *et al.* 2024a; Zhu *et al.* 2025). In contrast, numerous representative chromite deposits—such as those at Jiacha, Cuobuzha, and Renbu—have been discovered and studied within the southern Yarlung Zangbo Suture Zone (YZSZ) (Yang *et al.* 2022b; Hu *et al.* 2026; Lian *et al.* 2026).

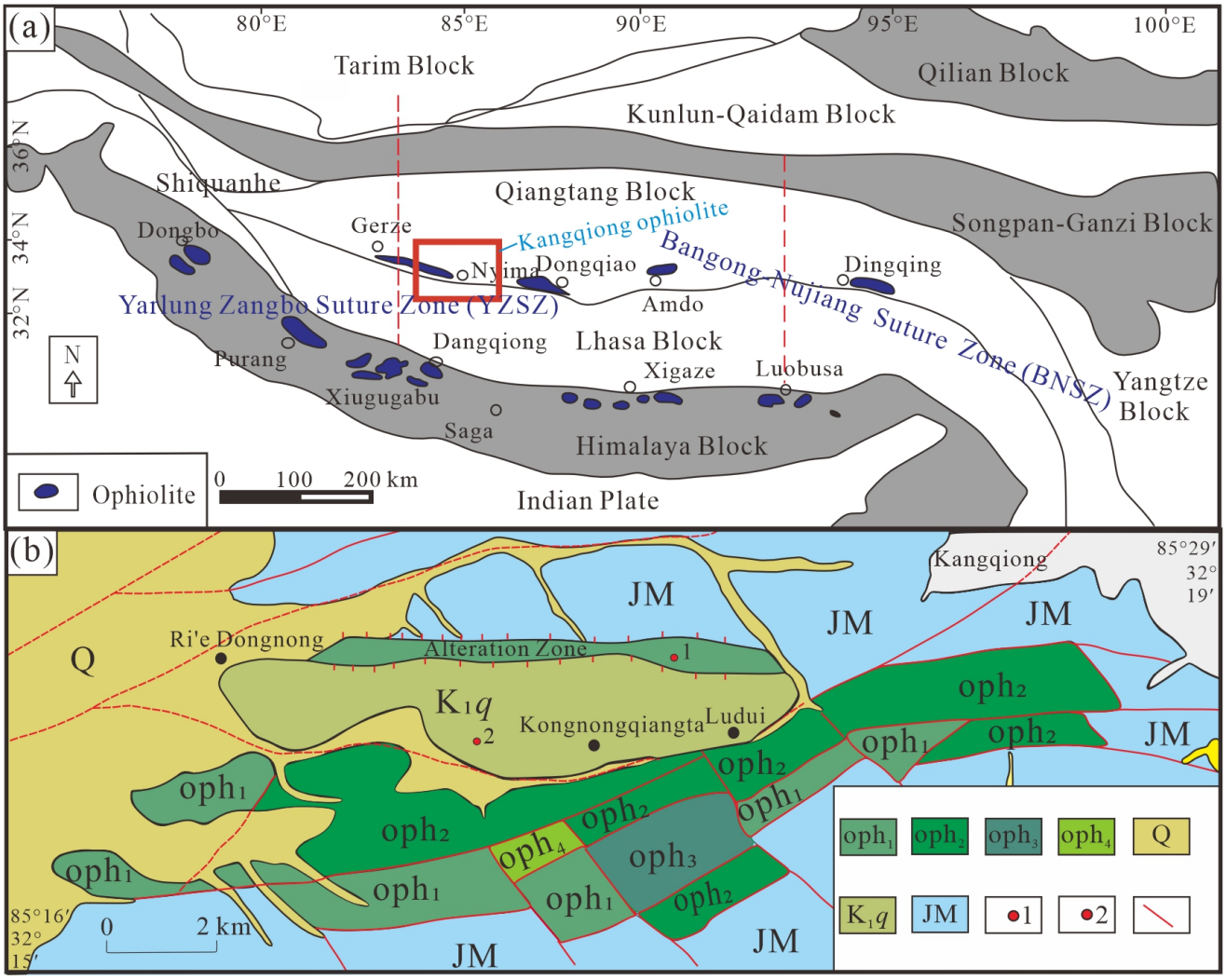



**Figure 1.** Simplified geological map and the Kangqiong ophiolite (modified after Shi *et al*. 2024; Zeng *et al.* 2021). Study area location. **(a)** Geological sketch map of the Bangong-Nujiang Suture Zone, Tibet; **(b)** Distribution map of ophiolites in the Kangqiong area (Q—Quaternary; $K_1q$—Qushenla Formation; JM—Mugagangri Group; $oph_1$—Peridotite; $oph_2$—Cumulate; $oph_3$—Mafic dike; $oph_4$—Pillow basalt; 1—Kangqiong chromitite; 2—Kongnongqiangta copper mineralization point; Fault). Abbreviations in the legend: $oph_1$, mantle peridotites; $oph_2$, mafic-ultramafic cumulates

## *2.2. Geology and petrography of the Kangqiong ophiolite*

During systematic field investigations and regional mapping conducted in 2012, a highly prospective podiform chromitite body was discovered along the highly sheared margins of an ultramafic rock mass in the Kangqiong area (Li *et al.* 2014) (Figure 1), effectively establishing the focal site for this present research. The dominant sedimentary sequence exposed throughout the regional Kangqiong sector is the Upper Jurassic to Lower Cretaceous Mugagangri Group. This massive rock group is primarily constituted by a deepsea to hemi-pelagic flysch formation, featuring rhythmic, turbiditic alternations of sandstones, siltstones, and heavily foliated slates. Interspersed chaotically throughout this fine-grained matrix are vast quantities of exotic tectonic blocks possessing highly heterogeneous chemical compositions and diverse geochronological ages, collectively exhibiting the textbook architectural hallmarks of a chaotic oceanic subduction accretionary wedge mélange. Studies of the Mugagangri Group at Gaize have documented extensional crack-seal veins in sandstone blocks of the broken formation; fluid-inclusion data indicate that these veins record fluid

flow during mélange formation and accretionary-wedge development (Liu *et al.* 2023).

The development of Early Cretaceous (~115 Ma) boninitic dikes in the Kangqiong ophiolite (Xu *et al.* 2015), along with magmatic records such as plagiogranites in the adjacent Gerze area (Fan *et al.* 2010), indicates that this region experienced a drastic dynamic transition from stable mid-ocean ridge spreading to intra-oceanic subduction initiation during the Early Cretaceous. Although direct geochronological constraints on the mantle-hosted chromitites are currently lacking—precluding a direct correlation with the absolute age of shallow crustal magmatic events—their low-Ti chromian-spinel compositions are compatible with a possible relationship to forearc SSZ magmatism, but do not establish an equivalent age or a direct genetic link to shallow crustal events. These chromitites not only fill the prospecting gap in this area but also provide a natural petrological probe for studying deep mantle evolution and metallogenic processes during subduction initiation (Zeng *et al.* 2021).

## 3. Characteristics of chromitites and host rocks

Ophiolites represent the stranded, solid-state remnants of paleo-oceanic lithosphere that, during the chaotic throes of subduction and ensuing orogenesis (Dilek and Furnes 2011), were structurally decoupled, and ultimately obducted onto continental margins, escaping the recycling fate of the deep mantle. The basal metamorphic mantle peridotite sequences of these complexes are not merely the volumetric bulk of the regional mélange belts; they serve as the direct, indispensable spatial reservoirs and active "melt-rock interaction" targets fundamentally required for the genesis of podiform chromitites (Xie *et al.* 2026; Tang *et al.* 2026). The Kangqiong chromitite does not exist as an isolated, anomalous geobody. Rather, its formation is intrinsically linked to the tectono-magmatic evolution of the broader ophiolite system; the podiform chromitites occur within the mantle section and are interpreted to have formed during the tectonic transition from a mid-ocean ridge to a subduction zone (Zhang, *et al.* 2024b; Xiong *et al.* 2025). Macroscopically, the ophiolitic host rocks and the chromite bodies constitute an indivisible, coherent metallogenic geological complex.

### *3.1. Petrological features of the Kangqiong ophiolite*

The Kangqiong and Ludui ophiolites in the central-western segment of the Bangong-Nujiang Suture Zone are key geological remnants that record the magmatic evolution and subduction history of the Meso-Tethys Ocean. As illustrated in the simplified geological map, the ophiolites in this belt generally trend east-west, extending for over ten kilometers with a maximum north-south width of approximately 4 kilometers and a total exposed area of about 30 square kilometers. Due to intense tectonic compression and dismemberment during the orogeny, continuous profiles of the oceanic lithosphere no longer exist. Instead, the various rock units primarily occur as fault-bounded tectonic blocks, exhibiting complex fault contacts with surrounding rocks such as the Jurassic Mugagangri Group (JM). Despite undergoing a high degree of tectonic stacking and disruption, the region still preserves a complete paleo-oceanic crustal sequence. The major lithological units occur as fault-bounded tectonic fragments within the ophiolitic mélange. Following Dilek and Furnes 2011, four core petrological end-members are recog-nized: the oceanic mantle basement of metamor-phosed mantle peridotites ($oph_1$); mafic–ultramafic cumulates represent-ting deep-magma-chamber products ($oph_2$); mafic dike swarms serving as shallow magmatic conduits ($oph_3$); and mafic pillow lavas resulting from seafloor eruptions ($oph_4$). This remarkable hybrid deformation structure and diverse magma end-member combinations provide a solid foundation for the formation mechanism of chromite.

### *3.2. Characteristics of the chromitite orebodies*

Spatially, the Kangqiong chromitite bodies predominantly occur within the alteration zones on the northern side of the ophiolite belt. Their host rocks are mainly harz-burgites that have undergone varying degrees of serpentinization and carbonatization. Macroscopic field investigations (Figure 2) reveal that the chromitite bodies generally occur as discontinuous lenses or typical podiform shapes. The largest known ore body extends up to 23 m along strike with a maximum width of ~2.7 m. Regarding ore structures, high-grade massive chromitites are the dominant type. Locally, network-vein and densely disseminated chromitites also occur. Petrographic observations under plane-polarized light indicate that chromian spinel grains are generally subhedral to anhedral and widely display cataclastic textures induced by late-stage tectonic deformation. Additionally, early-stage minute silicate inclusions are occasionally observed within some chromian spinel crystals. These features not only record the crystallization history of the primary magma but also reflect the complex structural superimposition and physicochemical modifications during the post-metallogenic stage.

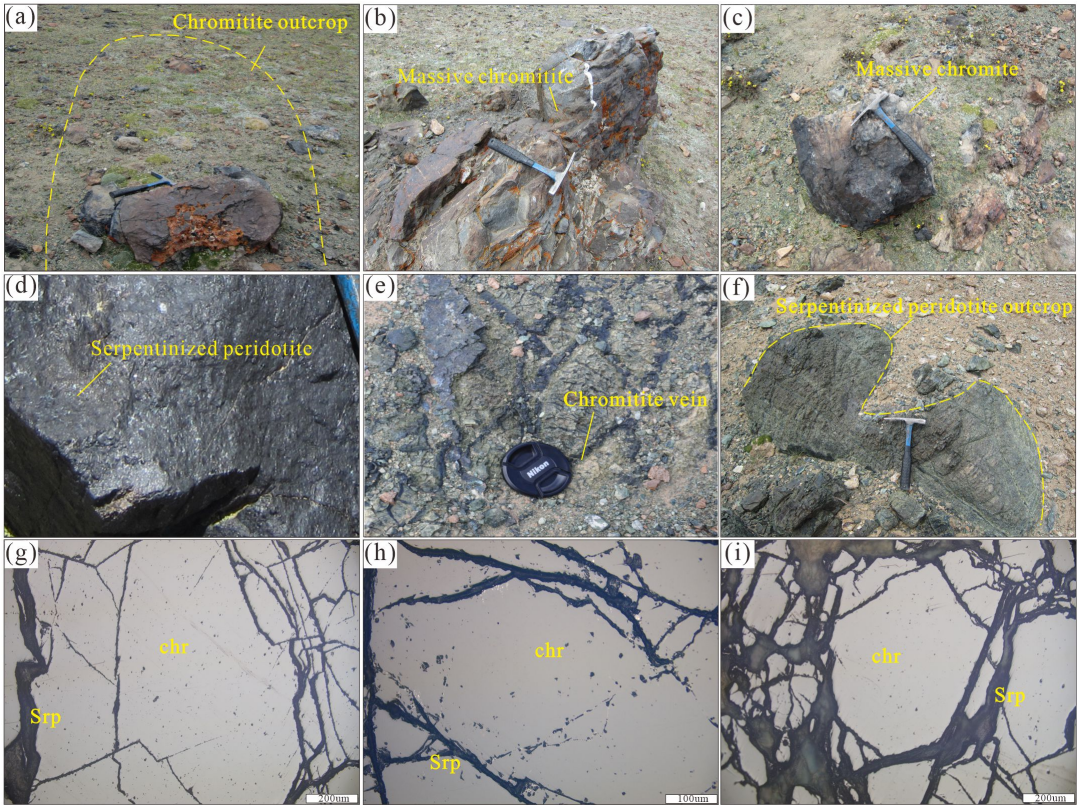



**Figure 2.** Field occurrences of chromitites and host peridotites in the Kangqiong ophiolite. **(a)** General view of the chromite outcrop; **(b, c)** Field outcrop and hand specimen of massive chromite; **(d)** A block of massive chromite overlying weathered serpentinized peridotite; **(e)** Network-vein chromite hosted within dunite; **(f)** Outcrop of serpentinized peridotite; **(g–i)** Photomicrographs of the chromitites taken under plane-polarized light. Mineral abbreviations: Chr, chromian spinel; Srp, secondary serpentine filling the interstitial fractures.

# 4. Analytical methods

## *4.1. Electron Probe Microanalysis (EPMA)*

The primary quantitative evaluation of major element concentrations within the Kangqiong chromitites and its immediate surrounding metamorphic peridotite hosts was executed utilizing state-of-the-art EPMA methodologies. The specific operational parameters for the microprobe were strictly calibrated to ensure maximum accuracy and minimize beam damage, utilizing an accelerating voltage of 15 kV, an operational beam current of 20 nA, and a tightly focused beam spot diameter constrained to approximately 1–2 μm. This narrow beam spot is essential to prevent spatial overlap and edge-effect contamination from adjacent silicate phases or microscopic inclusions. The highly technical execution of this analytical testing phase was commissioned to and completed by Beijing Gaonian Linghang Technology Co., Ltd. The meticulously acquired high-resolution data from this process serves to reliably decode the source attributes of the metallogenic magma, the extent of upper mantle partial melting, and the profound variations induced by late-stage magmatic evolution and cooling (Table 1).

## *4.2. Whole-rock geochemical analysis*

Prior to any chemical dissolution, the metamorphic peridotite samples retrieved from the Kangqiong ophiolitic mélange were subjected to rigorous noncontaminating mechanical crushing. Any weathered surfaces or late-stage calcite veins were physically removed before the samples were pulverized in an agate mill, achieving a uniform grain size of 200-mesh to ensure complete homogenization. The subsequent major and trace element quantifications were partitioned and executed independently at two facilities to ensure cross-laboratory verification: the Testing Institute of the Chinese Academy of Geological Sciences, and the Geoscience Experimental Center of the China University of Geosciences (Beijing) (Table 2; Table 3).

The determination of bulk major element mass fractions was accomplished using high-precision X-ray Fluorescence (XRF) spectrometry on fused glass disks, with analytical uncertainties restricted to less than 2%. The quantification of trace elements, with a specific focus

on the highly diagnostic rare earth elements (REE) and high field strength elements (HFSE), was performed leveraging a combination of Inductively Coupled Plasma Mass Spectrometry (ICP-MS) and Inductively Coupled Plasma Optical Emission Spectrometry (ICP-OES) following complete acid digestion in Teflon bombs. The analytical precision and relative errors for the trace element suites were generally constrained to below 5%. To ensure maximum data reliability, analytical reproducebility, and absolute quality control throughout the testing continuum,the analytical protocols strictly integrated and continuously monitored primary national standard reference materials (specifically GSR-2 and GSR-3).

# 5. Analytical results

## 5.1. Mineral chemistry of chromitites

The electron probe microanalysis (EPMA) results of the Kangqiong chromitites (Table 1) indicate that the spinels are mainly composed of $Cr_2O_3$, $Al_2O_3$, FeO and MgO. The $Mg^{\#}$ values of chromian spinels range from 56.93 to 59.51. The contents of $Al_2O_3$, MgO, and FeO are 17.29 wt.%–18.44 wt.%, 12.61 wt.%–13.78 wt.%, and 16.15 wt.%–17.45 wt.%, respectively. The $TiO_2$ content is extremely low, generally less than 0.3%, exhibiting a distinct low-Ti signature.

Chromian spinels from Kangqiong have $Mg^{\#}$ values (Mg/[Mg + $Fe^{2+}$] * 100]) of 56.93–59.51, lower than those commonly reported for primary Cr chromitites. In the absence of coexisting olivine compositional data, we utilize the elemental decoupling within the chromian spinels as robust evidence for subsolidus Fe-Mg exchange. As widely demonstrated by Arai 1994, trivalent cations (Cr, Al) in spinel are highly resistant to post-magmatic modification and preserve the primary melt signature, whereas divalent cations ($Fe^{2+}$, Mg) are highly susceptible to subsolidus re-equilibration. The EPMA data (Table 1) reveal exactly this strict geochemical decoupling: the relatively low $Mg^{\#}$ values are accompanied by $Cr^{\#}$ (65.06–66.58) and extremely low $TiO_2$ contents (0.12–0.28 wt.%). This unequivocally demonstrates that the low $Mg^{\#}$ is not a primary melt feature, but rather the product of post-magmatic subsolidus Fe-Mg exchange during cooling (Arai 1994). When the meticulously acquired EPMA dataset representing the Kangqiong chromitite is projected onto standardized structural environment discrimination diagrams for magmatic spinels (Figure 3), In the $Mg^{\#}$–$Cr^{\#}$ diagram (Figure 3a), the analysed chromian spinels plot within the forearc-peridotite field. $TiO_2$ *vs.* $Cr^{\#}$ diagram (Figure 3b): The data array forms a tight, linear distribution strictly parallel to the typical fractional melting trend of boninitic (BON) magmatic systems, which differs significantly from the evolutionary trajectories of MORB or Island Arc Tholeiites (IAT). $Cr^{\#}$ *vs.* NiO and $Al_2O_3$ *vs.* $TiO_2$ diagrams: The sample projections consistently fall within the defined fields for forearc peridotites and SSZ mantle peridotites, plotting completely separate from MORB-type mantle domains.

**Table 1.** Electron probe microanalysis (EPMA) results of the chromitites (oxide concentrations in wt.%).

| Sample | $Na_2O$ | $Al_2O_3$ | $SiO_2$ | FeO | $Cr_2O_3$ | MnO | NiO | MgO | $K_2O$ | CaO | $TiO_2$ | Total | $Fe^{3+}/\Sigma Fe$ | $Mg^{\#}$ | $Cr^{\#}$ |
|---|---|---|---|---|---|---|---|---|---|---|---|---|---|---|---|
| 2026KT01-Chr1-7 | 0.04 | 17.69 | 0.12 | 16.70 | 52.11 | 0.22 | 0.21 | 12.86 | - | - | 0.14 | 100.08 | 0.11 | 57.85 | 66.40 |
| 2026KT01-Chr1-8 | 0.05 | 18.31 | 0.01 | 16.28 | 52.97 | 0.21 | 0.12 | 12.61 | - | - | 0.19 | 100.74 | 0.04 | 58.00 | 65.99 |
| 2026KT01-Chr1-9 | 0.01 | 18.04 | - | 16.39 | 51.25 | 0.21 | 0.14 | 12.76 | - | - | 0.15 | 98.93 | 0.09 | 58.12 | 65.59 |
| 2026KT01-Chr1-10 | 0.01 | 18.44 | - | 16.57 | 51.18 | 0.26 | 0.16 | 13.19 | 0.01 | 0.01 | 0.13 | 99.95 | 0.13 | 58.66 | 65.06 |
| 2026KT01-Chr1-11 | 0.02 | 18.20 | 0.01 | 16.15 | 52.25 | 0.16 | 0.21 | 12.93 | 0.02 | - | 0.13 | 100.07 | 0.08 | 58.80 | 65.82 |
| 2026KT01-Chr1-12 | 0.06 | 18.11 | - | 16.18 | 51.52 | 0.14 | 0.17 | 13.01 | 0.01 | - | 0.19 | 99.39 | 0.11 | 58.90 | 65.62 |
| 2026KT01-Chr1-1 | - | 17.34 | 0.03 | 16.71 | 51.42 | 0.19 | 0.08 | 13.78 | 0.01 | - | 0.15 | 99.69 | 0.19 | 59.51 | 66.55 |
| 2026KT01-Chr1-2 | 0.02 | 17.54 | 0.02 | 16.53 | 51.69 | 0.20 | 0.14 | 12.74 | - | - | 0.13 | 99.01 | 0.11 | 57.87 | 66.41 |
| 2026KT01-Chr1-3 | - | 17.47 | - | 16.45 | 51.87 | 0.20 | 0.16 | 12.79 | - | - | 0.16 | 99.11 | 0.10 | 58.09 | 66.58 |
| 2026KT01-Chr1-4 | - | 17.53 | - | 16.77 | 51.78 | 0.07 | 0.15 | 12.75 | 0.01 | - | 0.12 | 99.18 | 0.11 | 57.54 | 66.46 |
| 2026KT01-Chr1-5 | - | 17.50 | - | 16.39 | 51.60 | 0.23 | 0.13 | 12.69 | 0.01 | - | 0.14 | 98.69 | 0.10 | 57.99 | 66.42 |
| 2026KT01-Chr1-6 | - | 17.29 | 0.04 | 17.18 | 51.19 | 0.27 | 0.15 | 12.74 | 0.01 | - | 0.14 | 99.00 | 0.14 | 56.93 | 66.51 |
| 2026KT01-Chr2-7 | 0.02 | 17.77 | 0.01 | 17.36 | 50.50 | 0.19 | 0.07 | 13.47 | - | - | 0.18 | 99.58 | 0.19 | 58.04 | 65.59 |
| 2026KT01-Chr2-8 | 0.01 | 17.71 | - | 17.45 | 49.86 | 0.43 | 0.11 | 13.40 | - | - | 0.22 | 99.19 | 0.21 | 57.78 | 65.38 |
| 2026KT01-Chr2-9 | 0.06 | 17.77 | 0.03 | 16.50 | 51.05 | 0.18 | 0.07 | 13.46 | - | - | 0.22 | 99.33 | 0.16 | 59.25 | 65.84 |
| 2026KT01-Chr2-10 | - | 17.78 | 0.02 | 16.58 | 50.72 | 0.23 | 0.06 | 13.41 | 0.01 | - | 0.28 | 99.07 | 0.15 | 59.05 | 65.68 |
| 2026KT01-Chr2-11 | - | 17.81 | 0.04 | 17.14 | 50.13 | 0.32 | 0.16 | 13.67 | 0.01 | 0.01 | 0.24 | 99.51 | 0.20 | 58.71 | 65.38 |
| 2026KT01-Chr2-12 | 0.02 | 17.91 | - | 16.63 | 50.54 | 0.17 | 0.17 | 13.54 | 0.01 | - | 0.22 | 99.21 | 0.17 | 59.21 | 65.43 |
| 2026KT01-Chr2-1 | 0.01 | 17.77 | 0.04 | 16.86 | 51.06 | 0.28 | 0.12 | 13.25 | - | - | 0.25 | 99.63 | 0.15 | 58.35 | 65.84 |
| 2026KT01-Chr2-2 | - | 17.81 | - | 16.80 | 50.56 | 0.15 | 0.25 | 13.30 | 0.01 | 0.01 | 0.25 | 99.13 | 0.16 | 58.53 | 65.57 |
| 2026KT01-Chr2-3 | - | 17.71 | 0.02 | 16.67 | 51.08 | 0.16 | 0.13 | 13.17 | - | - | 0.23 | 99.16 | 0.13 | 58.48 | 65.93 |
| 2026KT01-Chr2-4 | 0.02 | 17.84 | 0.01 | 16.67 | 50.31 | 0.27 | 0.26 | 13.31 | 0.01 | - | 0.20 | 98.91 | 0.17 | 58.73 | 65.42 |
| 2026KT01-Chr2-5 | 0.04 | 17.68 | 0.04 | 16.84 | 51.13 | 0.20 | 0.21 | 13.27 | 0.02 | 0.01 | 0.20 | 99.63 | 0.16 | 58.41 | 65.99 |
| 2026KT01-Chr2-6 | - | 18.11 | 0.04 | 16.57 | 50.27 | 0.12 | 0.24 | 13.66 | 0.01 | - | 0.20 | 99.21 | 0.17 | 59.51 | 65.06 |

"-": below detection limit.

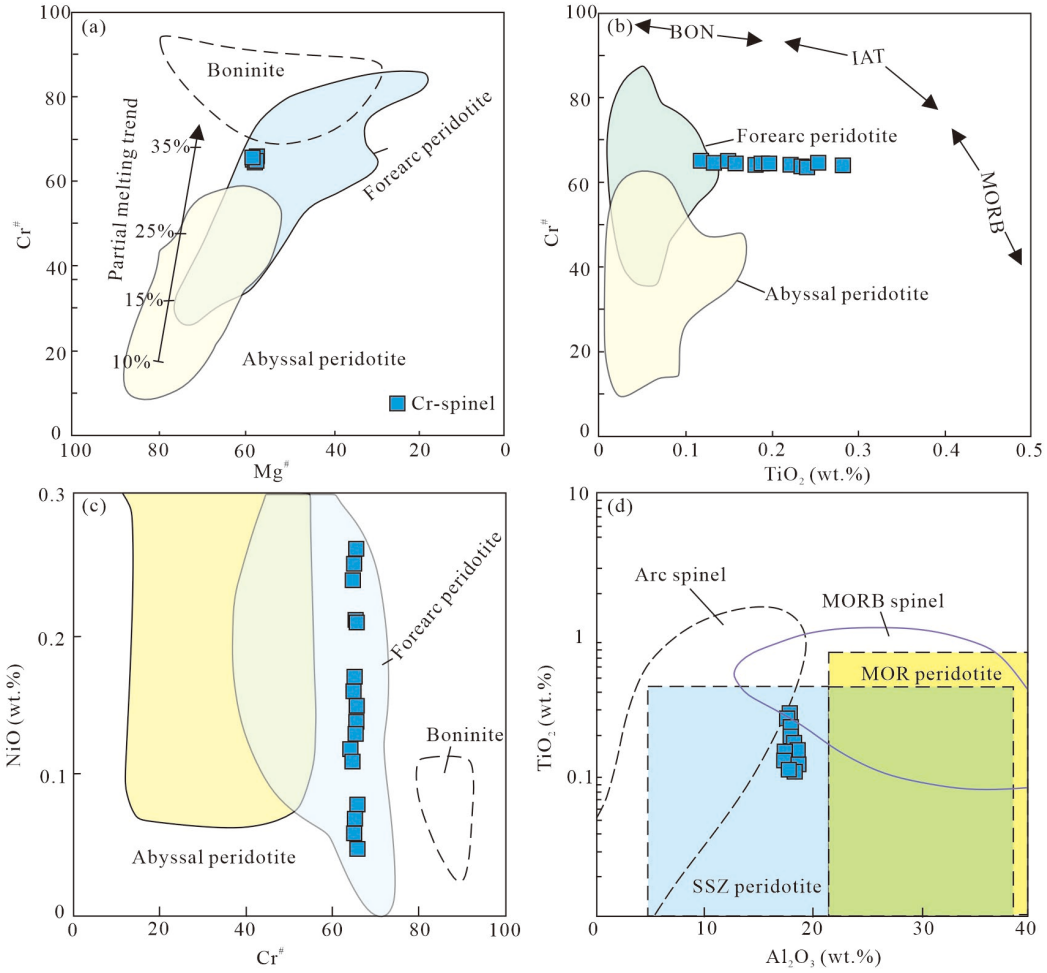



**Figure 3.** Diagrams showing the composition of spinel in chromitite from the Kangqiong area. **(a)** Cr# *vs.* Mg# diagram (Arai 1997); **(b)** Cr# *vs.* $TiO_2$ diagram (Pearce *et al.* 2000); **(c)** NiO *vs.* Cr# diagram (Wang *et al.* 2023); **(d)** $TiO_2$ *vs.* $Al_2O_3$ diagram (Miladinova *et al*. 2023).

## *5.2. Major and trace element characteristics of metamorphic peridotites*

The major element profiles of the Kangqiong metamorphic peridotites exhibit a typical ultramafic geochemical signature, representing the refractory residue after high degrees of basaltic melt extraction. The bulk $SiO_2$ compositions range from 38.23 wt.% to 47.53 wt.%. Significantly, MgO mass fractions are consistently high across the sample suite (30.50 wt.% to 37.17 wt.%), confirming a deep mantle provenance Conversely, the concentrations of highly incompatible, fusible components are profoundly suppressed. $Al_2O_3$ contents present remarkably low values, generally confined between 0.29 wt.% and 5.64 wt.%, while $TiO_2$ concentrations border on extreme trace levels, spanning a mere 0.01 wt.% to 0.03 wt.%.

Relying upon these elemental parameters, stoichiometric calculation dictates exceptionally high bulk rock $Mg^{\#}$ values fluctuating between 88.92 and 93.16, indicating extreme depletion. Based on their chondrite-normalized REE patterns, the samples are divided into two groups, Groups A and B (Figure 4; Table 2; Table 3).

Group A: These samples are characterized by extremely low total rare earth element (REE) concentrations. Their chondrite-normalized REE patterns display a typical "left-leaning" geometry, marked by severe depletion in light rare earth elements (LREEs) and relatively flat heavy rare earth element HREE patterns. In primitive mantle-normalized trace element spidergrams, Group A exhibits a generally low HFSE abundances and variable concentrations of fluid-mobile elements. These low REE abundances are consistent with melt depletion, representing a refractory mantle residue.

Group B: While maintaining low total REE concentrations similar to Group A, Group B exhibits noticeable anomalous enrichment in LREEs. This elevates the normalized curves into flattened or typical "U-shaped" patterns, which classically indicate late-stage fluid metasomatism. In the trace element spidergrams, Group B samples show low total REE concentrations and variable chondrite-normalized REE patterns, including relatively flat to U-shaped patterns (Figure 4c). Ba and Sr concentrations range from 0.99 to 6.85 ppm and from 1.12 to 4.37 ppm, respectively (Table 2; Table 3). HFSE abundances remain low (Figure 4d).

**Table 2.** Whole-rock geochemical results of the metamorphic peridotites from the Kangqiong ophiolitic mélange.

| Sample | T20H1 | T20H2 | T20H3 | T20H4 | T20H5 | T20H6 | T20H7 | T20H8 | T20H9 | T20H10 |
|---|---|---|---|---|---|---|---|---|---|---|
| **Major elements (wt.%)** | | | | | | | | | | |
| $SiO_2$ | 40.97 | 40.77 | 40.44 | 41.60 | 41.46 | 40.98 | 42.27 | 39.70 | 38.23 | 40.57 |
| $TiO_2$ | 0.01 | 0.01 | 0.02 | 0.03 | 0.03 | 0.01 | 0.02 | 0.03 | 0.01 | 0.02 |
| $Al_2O_3$ | 0.43 | 0.29 | 0.35 | 0.61 | 0.43 | 0.47 | 0.38 | 0.36 | 0.53 | 1.24 |
| $TFe_2O_3$ | 7.29 | 6.43 | 6.71 | 6.13 | 7.22 | 7.04 | 6.85 | 6.65 | 7.60 | 6.56 |
| MnO | 0.10 | 0.10 | 0.10 | 0.09 | 0.10 | 0.10 | 0.10 | 0.10 | 0.11 | 0.10 |
| MgO | 34.83 | 36.10 | 35.40 | 35.84 | 34.87 | 35.34 | 33.90 | 37.17 | 36.99 | 35.90 |
| CaO | 0.19 | 0.22 | 0.28 | 0.17 | 0.10 | 0.23 | 0.09 | 0.24 | 0.10 | 0.66 |
| Sample | T20H1 | T20H2 | T20H3 | T20H4 | T20H5 | T20H6 | T20H7 | T20H8 | T20H9 | T20H10 |
| **Major elements (wt.%)** | | | | | | | | | | |
| $Na_2O$ | 0.01 | 0.01 | 0.01 | 0.01 | 0.01 | 0.01 | 0.01 | 0.01 | 0.01 | 0.02 |
| $K_2O$ | 0.01 | 0.01 | 0.01 | 0.01 | - | 0.01 | 0.01 | 0.01 | 0.01 | - |
| LOI | 16.08 | 16.01 | 16.62 | 15.42 | 15.69 | 15.74 | 16.23 | 15.70 | 16.43 | 14.89 |
| SUM | 99.92 | 99.95 | 99.94 | 99.92 | 99.91 | 99.93 | 99.87 | 99.99 | 100.02 | 99.96 |
| $Mg^{\#}$ | 91.76 | 92.90 | 92.48 | 93.16 | 91.84 | 92.13 | 92.02 | 92.87 | 91.90 | 92.73 |
| **Trace elements (ppm)** | | | | | | | | | | |
| La | 0.02 | 0.02 | 0.01 | 0.02 | 0.02 | 0.06 | 0.03 | 0.04 | 0.06 | 0.03 |
| Ce | 0.02 | 0.02 | 0.01 | 0.02 | 0.02 | 0.10 | 0.08 | 0.07 | 0.09 | 0.06 |
| Pr | 0.01 | 0.01 | - | 0.01 | 0.01 | 0.02 | 0.01 | 0.01 | 0.02 | 0.01 |
| Nd | 0.04 | 0.03 | 0.02 | 0.04 | 0.03 | 0.07 | 0.04 | 0.05 | 0.08 | 0.09 |
| Sm | 0.01 | 0.01 | 0.01 | 0.01 | 0.01 | 0.02 | 0.01 | 0.02 | 0.02 | 0.03 |
| Eu | - | - | - | - | - | - | - | - | 0.01 | 0.01 |
| Gd | 0.02 | 0.01 | 0.01 | 0.01 | 0.02 | 0.02 | 0.01 | 0.02 | 0.03 | 0.05 |
| Tb | - | - | - | - | - | - | - | - | 0.01 | 0.01 |
| Dy | 0.02 | 0.02 | 0.01 | 0.02 | 0.03 | 0.03 | 0.03 | 0.03 | 0.04 | 0.07 |
| Ho | 0.01 | - | - | 0.01 | 0.01 | 0.01 | 0.01 | 0.01 | 0.01 | 0.02 |
| Er | 0.02 | 0.01 | 0.01 | 0.02 | 0.02 | 0.02 | 0.02 | 0.02 | 0.03 | 0.05 |
| Tm | - | - | - | - | - | - | - | - | 0.01 | 0.01 |
| Yb | 0.02 | 0.02 | 0.01 | 0.03 | 0.02 | 0.03 | 0.02 | 0.03 | 0.04 | 0.06 |
| Lu | - | - | - | - | - | 0.01 | - | 0.01 | 0.01 | 0.01 |
| Hf | 0.01 | 0.01 | 0.01 | 0.01 | 0.01 | 0.01 | 0.01 | 0.02 | 0.01 | 0.01 |
| Ta | 0.02 | 0.03 | 0.03 | 0.04 | 0.04 | 0.02 | 0.03 | 0.03 | 0.01 | 0.01 |
| Pb | 0.46 | 0.57 | 0.34 | 0.30 | 0.23 | 0.38 | 0.36 | 0.19 | 0.98 | 0.57 |
| Th | 0.01 | 0.01 | 0.01 | 0.01 | 0.01 | 0.01 | 0.01 | - | 0.01 | 0.01 |
| **Trace elements (ppm)** | | | | | | | | | | |
| U | 0.01 | 0.01 | 0.01 | - | 0.01 | 0.01 | 0.01 | 0.01 | 0.02 | 0.01 |
| Ni | 1268 | 1324 | 1229 | 1794 | 1398 | 1226 | 1211 | 1655 | 1304 | 1631 |
| Rb | 0.32 | 0.21 | 0.20 | 0.14 | 0.14 | 0.33 | 0.17 | 0.20 | 0.38 | 0.20 |
| Sr | 1.63 | 1.98 | 1.77 | 1.74 | 1.12 | 3.52 | 1.19 | 1.38 | 3.48 | 4.37 |
| Y | 0.12 | 0.09 | 0.05 | 0.10 | 0.10 | 0.16 | 0.07 | 0.15 | 0.18 | 0.37 |
| Zr | 0.58 | 0.48 | 0.43 | 0.50 | 0.47 | 0.50 | 0.51 | 0.66 | 0.61 | 0.53 |
| Nb | 0.29 | 0.35 | 0.52 | 0.53 | 0.54 | 0.17 | 0.46 | 0.47 | 0.16 | 0.12 |
| Ba | 1.12 | 0.99 | 3.44 | 1.45 | 0.99 | 5.46 | 1.13 | 1.15 | 6.85 | 2.31 |

**Table 3.** Whole-rock geochemical results of the metamorphic peridotites from the Kangqiong ophiolitic mélange.

| Sample | P16H1 | P16H2 | P16H3 | P16H4 | P16H5 | P12H1 | P12H2 | P12H3 | P12H4 | P12H5 | T19H6 |
|---|---|---|---|---|---|---|---|---|---|---|---|
| **Major elements (wt.%)** | | | | | | | | | | | |
| $SiO_2$ | 45.46 | 46.14 | 45.45 | 47.05 | 46.86 | 45.48 | 47.53 | 43.29 | 45.52 | 45.86 | 44.55 |
| $TiO_2$ | 0.01 | 0.02 | 0.02 | 0.02 | 0.03 | 0.03 | 0.02 | 0.02 | 0.03 | 0.03 | 0.03 |
| $Al_2O_3$ | 5.64 | 5.23 | 5.44 | 5.34 | 4.63 | 3.30 | 1.87 | 5.43 | 3.69 | 2.98 | 0.63 |
| $TFe_2O_3$ | 8.39 | 8.00 | 8.30 | 7.97 | 8.36 | 8.69 | 9.57 | 9.23 | 8.88 | 9.27 | 8.01 |
| MnO | 0.12 | 0.11 | 0.11 | 0.11 | 0.12 | 0.13 | 0.13 | 0.13 | 0.13 | 0.14 | 0.09 |
| Sample | P16H1 | P16H2 | P16H3 | P16H4 | P16H5 | P12H1 | P12H2 | P12H3 | P12H4 | P12H5 | T19H6 |
| **Major elements (wt.%)** | | | | | | | | | | | |
| MgO | 31.69 | 30.65 | 32.05 | 30.50 | 31.76 | 34.11 | 33.20 | 34.99 | 33.50 | 31.92 | 33.07 |
| CaO | 2.81 | 3.61 | 3.06 | 3.30 | 1.99 | 2.98 | 3.82 | 4.35 | 4.70 | 5.75 | 0.10 |
| $Na_2O$ | 0.01 | 0.02 | 0.02 | 0.02 | 0.02 | 0.02 | 0.08 | 0.18 | 0.06 | 0.05 | 0.02 |
| $K_2O$ | - | - | - | - | - | - | - | 0.01 | - | - | - |
| LOI | 5.92 | 6.11 | 5.62 | 5.47 | 6.02 | 5.29 | 3.47 | 3.18 | 3.61 | 3.93 | 13.32 |
| SUM | 100.06 | 99.89 | 100.08 | 99.79 | 99.78 | 100.03 | 99.69 | 100.82 | 100.13 | 99.94 | 99.82 |
| $Mg^{\#}$ | 89.80 | 89.93 | 90.00 | 89.92 | 89.85 | 90.14 | 88.99 | 89.83 | 89.79 | 88.92 | 90.60 |
| **Trace elements (ppm)** | | | | | | | | | | | |
| La | 0.01 | 0.02 | 0.01 | 0.01 | 0.02 | 0.04 | 0.04 | 0.11 | 0.04 | 0.03 | 0.04 |
| Ce | 0.04 | 0.06 | 0.05 | 0.06 | 0.08 | 0.11 | 0.20 | 0.24 | 0.12 | 0.10 | 0.10 |
| Pr | 0.01 | 0.01 | 0.01 | 0.01 | 0.01 | 0.02 | 0.02 | 0.03 | 0.02 | 0.02 | 0.02 |
| Nd | 0.04 | 0.05 | 0.06 | 0.07 | 0.08 | 0.09 | 0.08 | 0.13 | 0.09 | 0.10 | 0.10 |
| Sm | 0.02 | 0.03 | 0.03 | 0.04 | 0.04 | 0.05 | 0.04 | 0.04 | 0.05 | 0.05 | 0.04 |
| Eu | 0.01 | 0.02 | 0.02 | 0.02 | 0.02 | 0.02 | 0.02 | 0.02 | 0.02 | 0.03 | 0.02 |
| Gd | 0.03 | 0.05 | 0.06 | 0.07 | 0.08 | 0.10 | 0.07 | 0.06 | 0.09 | 0.11 | 0.08 |
| Tb | 0.01 | 0.01 | 0.01 | 0.01 | 0.02 | 0.02 | 0.02 | 0.01 | 0.02 | 0.03 | 0.01 |
| Dy | 0.04 | 0.07 | 0.09 | 0.10 | 0.11 | 0.15 | 0.11 | 0.08 | 0.15 | 0.20 | 0.10 |
| Ho | 0.01 | 0.02 | 0.02 | 0.02 | 0.02 | 0.04 | 0.03 | 0.02 | 0.04 | 0.05 | 0.02 |
| Er | 0.03 | 0.05 | 0.06 | 0.07 | 0.08 | 0.12 | 0.08 | 0.06 | 0.12 | 0.15 | 0.07 |
| Tm | 0.01 | 0.01 | 0.01 | 0.01 | 0.01 | 0.02 | 0.02 | 0.01 | 0.02 | 0.02 | 0.01 |
| Yb | 0.03 | 0.05 | 0.05 | 0.07 | 0.08 | 0.13 | 0.09 | 0.07 | 0.12 | 0.16 | 0.06 |
| Lu | 0.01 | 0.01 | 0.01 | 0.01 | 0.01 | 0.02 | 0.02 | 0.01 | 0.02 | 0.03 | 0.01 |
| Hf | 0.01 | 0.01 | 0.01 | 0.02 | 0.02 | 0.03 | 0.02 | 0.02 | 0.03 | 0.03 | 0.02 |
| Ta | 0.02 | 0.02 | 0.02 | 0.01 | 0.01 | 0.02 | 0.02 | 0.01 | 0.02 | 0.02 | 0.02 |
| Pb | 0.01 | 0.01 | 0.01 | 0.06 | 0.39 | 0.45 | 1.53 | 0.11 | 2.54 | 1.36 | 0.03 |
| Th | 0.02 | 0.02 | 0.02 | 0.02 | 0.04 | 0.07 | 0.05 | 0.07 | 0.09 | 0.06 | 0.01 |
| U | - | 0.01 | - | 0.01 | 0.01 | 0.02 | 0.02 | 0.01 | 0.03 | 0.02 | 0.01 |
| Ni | 1316 | 1228 | 1348 | 1213 | 1280 | 1529 | 1525 | 1546 | 1418 | 1304 | 1001 |
| Rb | 0.43 | 0.34 | 0.27 | 0.32 | 0.17 | 0.13 | 0.20 | 0.19 | 0.17 | 0.13 | 0.12 |
| Sample | P16H1 | P16H2 | P16H3 | P16H4 | P16H5 | P12H1 | P12H2 | P12H3 | P12H4 | P12H5 | T19H6 |
| **Trace elements (ppm)** | | | | | | | | | | | |
| Sr | 3.89 | 4.80 | 2.56 | 3.43 | 3.56 | 5.96 | 15.02 | 15.55 | 11.61 | 8.27 | 2.25 |
| Y | 0.22 | 0.38 | 0.45 | 0.55 | 0.60 | 0.91 | 0.61 | 0.43 | 0.90 | 1.19 | 0.51 |
| Zr | 0.53 | 0.55 | 0.44 | 0.71 | 0.91 | 0.94 | 0.93 | 0.82 | 1.18 | 0.94 | 0.93 |
| Nb | 0.25 | 0.22 | 0.29 | 0.20 | 0.19 | 0.27 | 0.25 | 0.13 | 0.32 | 0.31 | 0.25 |
| Ba | 0.61 | 1.31 | 0.50 | 0.62 | 0.78 | 35.20 | 1.55 | 3.44 | 4.56 | 1.88 | 1.63 |

"-": below detection limit.

Analytical laboratory: China University of Geosciences (Beijing).

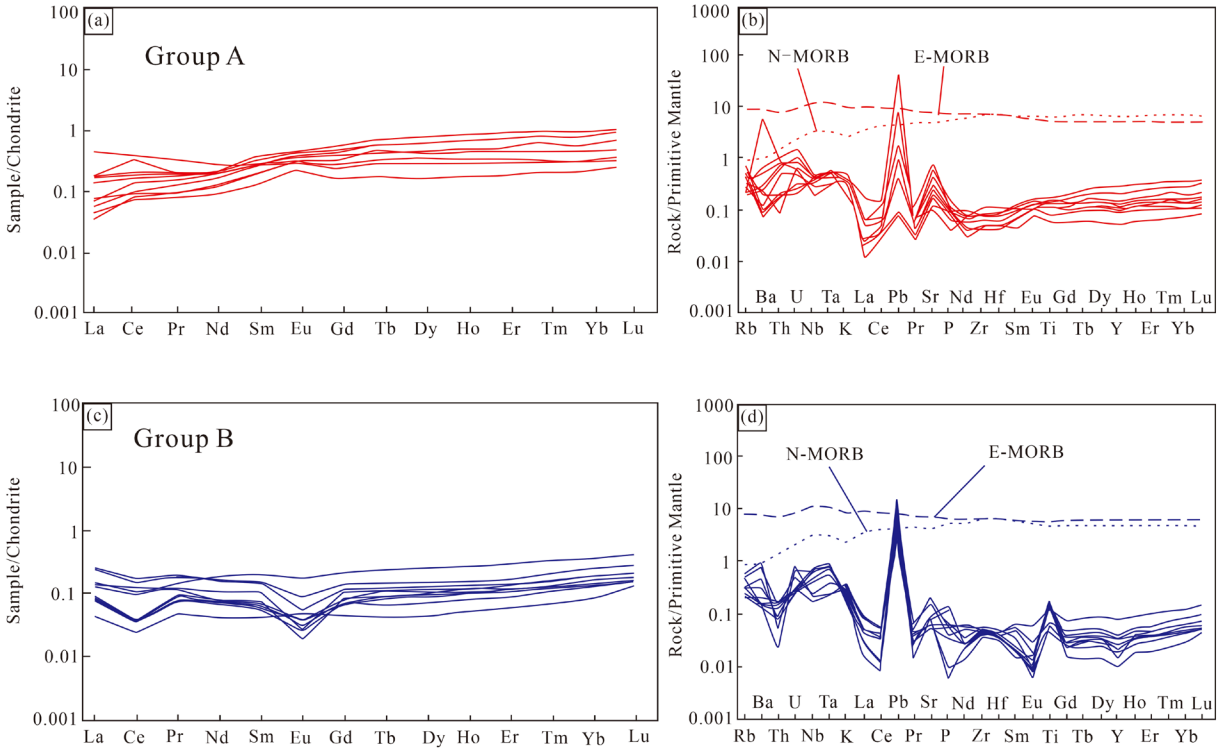



**Figure 4.** Chondrite-normalized REE patterns **(a, c)** and primitive mantle-normalized trace element spider diagrams **(b, d)** for metaperidotites from the Kangqiong area. Panels **(a)** and **(b)** represent Group A; panels **(c)** and **(d)** represent Group B. Chondrite normalization values are after Boynton 1984. Primitive mantle, N-MORB (Normal Mid-Ocean Ridge Basalt), and E-MORB (Enriched Mid-Ocean Ridge Basalt) reference values are after Sun and McDonough 1989.

# 6. Discussion

## *6.1. Mantle source characteristics and possible fluid—rock modification of the metamorphic peridotites*

The metamorphic peridotites show contrasting major-element compositions in the CaO–$Al_2O_3$–MgO ternary diagram (Figure 5; Wafik *et al*. 2026 ). Group A samples predominantly plot within the Ultramafic Cumulate (UC) field and the transitional zone, whereas Group B samples plot closer to the MgO apex. Group A has relatively higher CaO and $Al_2O_3$ proportions, which could reflect differences in primary mineral proportions, crystal accumulation, or localized melt impregnation (Zhou *et al.* 1996; Zhang *et al.* 2024b). The diagram alone does not distinguish between a cumulate origin and modification of a residual mantle protolith, particularly given the alteration of the samples. Group B is relatively Mg-rich, and its depleted trace-element background is consistent with a melt-depleted mantle component. These compositional contrasts suggest that the host rocks have experienced a heterogeneous history of melt extraction and subsequent modification, rather than representing a uniform mantle residue. The depleted REE patterns provide additional constraints on this interpretation. Although REE can remain relatively immobile during serpentinization at the whole-rock scale (Deschamps *et al.* 2013), individual pattern features must be evaluated against REE-hosting minerals, possible redistribution, and element-specific detection limits and analytical uncertainties, especially at the low concentrations measured here.

Melt extraction followed by localized compositional modification therefore provides a plausible framework for interpreting the peridotites. Melt impregnation is one possible explanation for the Group A compositions, but its extent and the composition of the infiltrating melt are not quantitatively constrained. Fluid–rock interaction may also have contributed to the observed variability. The available whole-rock data do not establish the source or timing of that interaction, and later serpentinization and hydrothermal alteration remain possible contributors (Deschamps *et al.* 2013; Zhu *et al.* 2025).

To examine compositional variability associated with alteration, LOI was compared with Ba, Rb, Sr, U, and Pb concentrations within each sample group (Figure 6). The relationships vary among elements and groups, and no consistent linear trends are evident. However, the absence of such trends does not exclude alteration-related redistribution. Given the substantial alteration indicated by the LOI values, these fluid-mobile elements are not used to identify mantle metasomatism or a slab-derived component. Figure 6 documents the observed variability without establishing its origin or timing (Deschamps *et al.* 2013).

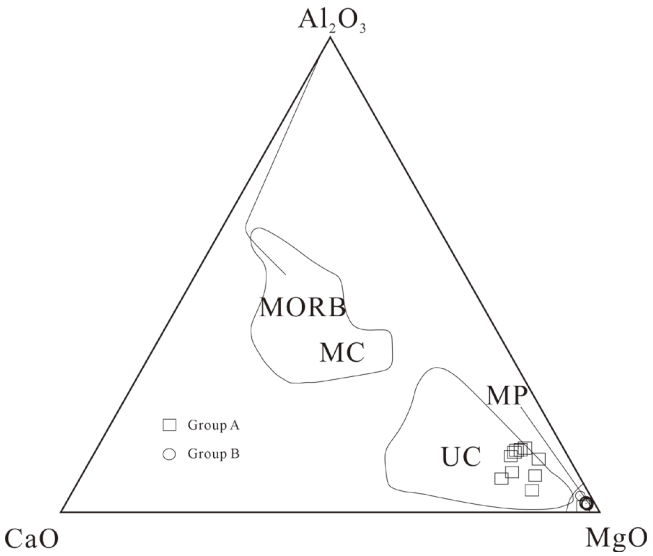



**Figure 5.** CaO-$Al_2O_3$-MgO ternary diagram for the Kangqiong mantle peridotites. Background fields for ultramafic cumulates and metamorphic peridotites are modified after Wafik *et al*. (2026). The solid line indicates the melt depletion trend. MC: Mafic cumulates; UC: Ultramafic cumulates; MP: Metaperidotites; MORB: Mid-Ocean Ridge Basalt.

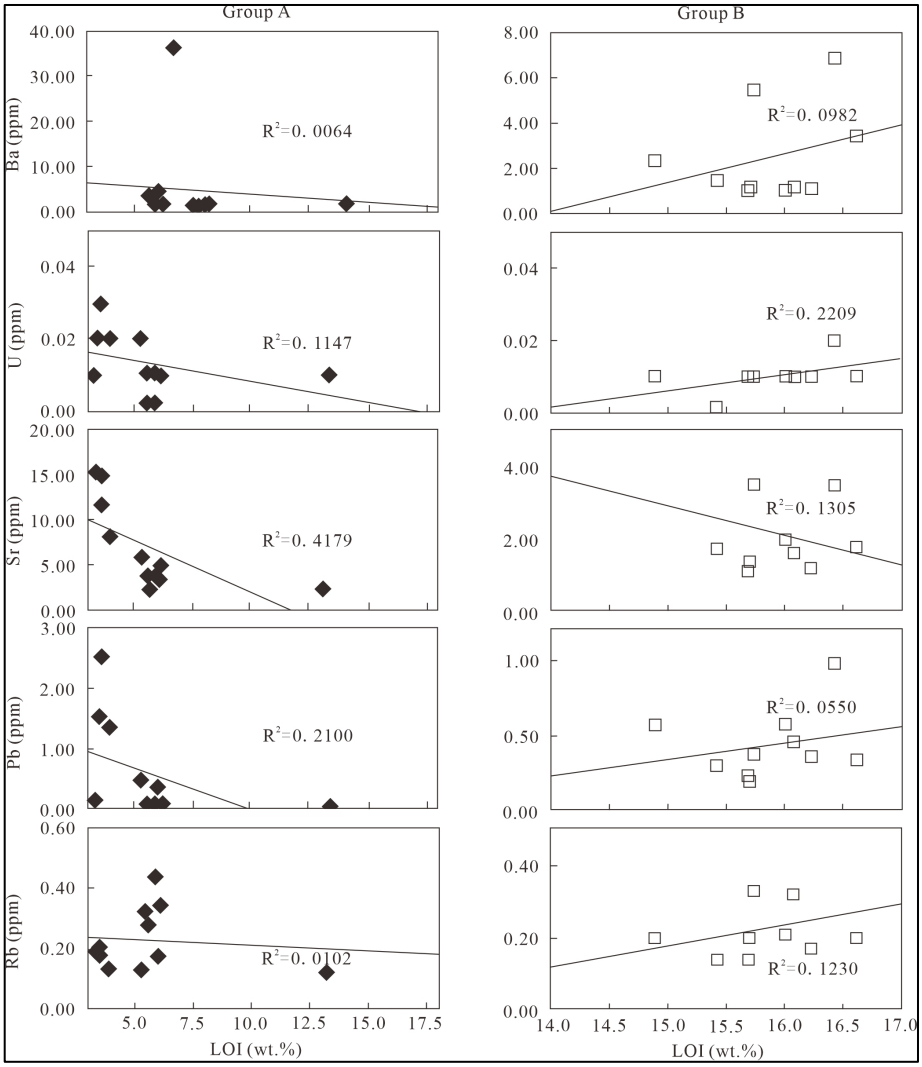



**Figure 6.** Scatter plots of Loss on Ignition (LOI) versus fluid-mobile elements (Ba, U, Sr, Pb, and Rb) for the Kangqiong mantle peridotites. Group A is shown in the left column (solid diamonds), and Group B in the right column (open squares). $R^2$ values are the coefficients of determination for the corresponding linear regressions.

### 6.2. Melt–rock interaction and chromitite formation

Chromian spinel provides mineral-chemical constraints on the parental-melt affinity and tectonic setting of the Kangqiong chromitites. The samples have $Cr^{\#}$ values of 65.06–66.58, $Mg^{\#}$ values of 56.93–59.51, and $TiO_2$ contents of 0.12–0.28 wt.%. In the $Mg^{\#}$–$Cr^{\#}$ diagram (Figure 3a), their compositions plot within the forearc-peridotite field. This distribution is consistent with a forearc-related interpretation, but does not independently establish a boninitic parental melt. The tectonic interpretation therefore considers the $Cr^{\#}$ values, low $TiO_2$ contents, the other discrimination diagrams, and the regional geological setting together (Arai 1994, 1997; Pearce *et al.* 2000). Because Mg# can be influenced by cooling and post-magmatic re-equilibration, it is evaluated together with these other indicators (Kamenetsky *et al.* 2001).

Using the stoichiometric criteria of Droop 1987, we recalculated the $Fe^{3+}$ contents of chromian spinel from the EPMA data. The resulting $Fe^{3+}/\Sigma Fe$ ratios range from 0.044 to 0.210, with an average of 0.140. These values represent estimated ferric-iron proportions under the assumptions of stoichiometric recalculation rather than a direct determination of oxygen fugacity ($fO_2$). Their interpretation requires consideration of analytical uncertainty and possible post-magmatic modification. The ratios are reported as part of the spinel compositional dataset, but they are not treated as independent evidence for highly oxidized crystallization conditions or an SSZ setting.

Taken together, the $Cr^{\#}$ values, low $TiO_2$ contents, discrimination-diagram relationships, and regional geological context favour an SSZ-related interpretation for the Kangqiong chromitites. A parental melt with possible boninitic affinity provides a plausible explanation for this combination of features. Comparisons with other chromitites and published models provide context for this interpretation (Zhou *et al.* 2014; Zhang *et al.* 2024a; Zhang P, *et al.* 2024b), although the present mineral-chemical data do not uniquely determine the melt composition, degree of partial melting, or contribution of slab-derived fluids.

Melt–rock interaction provides a possible link between the inferred parental-melt affinity and chromitite formation. In the proposed model, migrating melt interacted with depleted mantle peridotite. If the melt was undersaturated with respect to orthopyroxene, dissolution of this mineral and crystallization of olivine could have modified the melt composition and contributed to the development of dunite reaction zones. This reaction pathway is consistent with published models of podiform chromitite formation (Zhou *et al.* 1994; Arai and Miura 2016). Here, the association with dunite is consistent with melt–rock interaction, although the origin of the dunite and the detailed reaction pathway remain unconstrained.

Changes in melt composition during reaction with peridotite can promote chromite saturation and accumulation, providing a reasonable mechanism for the formation of the Kangqiong chromitite bodies (Zhou *et al.* 1996; González-Jiménez *et al.* 2014). The combined mineral-chemical and host-rock observations make melt-rock interaction a plausible petrogenetic interpretation and provide a plausible mechanism for chromitite formation, while the detailed reaction sequence remains to be tested.

### 6.3. Proposed two-stage tectono-magmatic evolution

The Kangqiong chromitites can be considered alongside other chromitite occurrences in the Bangong–Nujiang Suture Zone, including Jiangco, Dongqiao, and Dingqing. Studies of these occurrences provide a regional context for discussing mantle evolution and melt–rock interaction (Xie *et al.* 2025; Tang *et al.* 2026). At Kangqiong, the Early Cretaceous boninitic dikes reported by Xu *et al.* (2015), with ages of approximately 115 Ma, provide evidence of regional boninitic magmatism. The mineral-chemical affinity inferred for the chromitites is compatible with this broader SSZ-related context. However, the similarity does not establish that the chromitites and dikes were coeval or genetically linked. Regional reconstructions of the Bangong–Nujiang Ocean constrain the tectonic framework rather than the formation age of the chromitites themselves (Li *et al.* 2026; Liu *et al.* 2026).

We propose a two-stage tectono-magmatic model that links the host-rock compositional heterogeneity and chromitite mineral chemistry to this regional framework (Figure 7). The model draws on published interpretations of melt–rock interaction and mantle evolution during subduction initiation (Zhou *et al.* 1996; Dilek and Furnes 2011; Zhang *et al*. 2024b).

Stage 1: Proposed MOR-Type Mantle Evolution. An early episode of mantle melting and melt extraction established a depleted mantle framework. Localized interaction with migrating melts subsequently modified parts of this framework (Dilek and Furnes 2011; Zhang P *et al.* 2024b). Within the model, a residual mantle protolith followed by melt impregnation provides one possible interpretation of the Group A compositions. This interpretation accommodates its depleted trace-element signatures and major-element variability, while a cumulate origin remains an alternative requiring mineralogical and textural evaluation.

Stage 2: Proposed SSZ-Related Magmatism and Chromitite Formation. Subsequent magmatism in an SSZ setting supplied melts of possible boninitic affinity that interacted with mantle peridotite and promoted chromian-spinel saturation and accumulation (Zhou *et al.* 1996; Zhang *et al.* 2024b). Fluid-assisted melting is a possible part of this regional model, but the Group B whole-rock compositions do not independently establish a slab-derived fluid source. The Early Cretaceous dikes provide a regional temporal reference for this stage;

the age of chromitite formation remains unconstrained (Xu *et al.* 2015). Thus, the two-stage model offers an integrated interpretation of the mineral-chemical and host-rock observations, with the protolith relationships and timing remaining open to further testing.

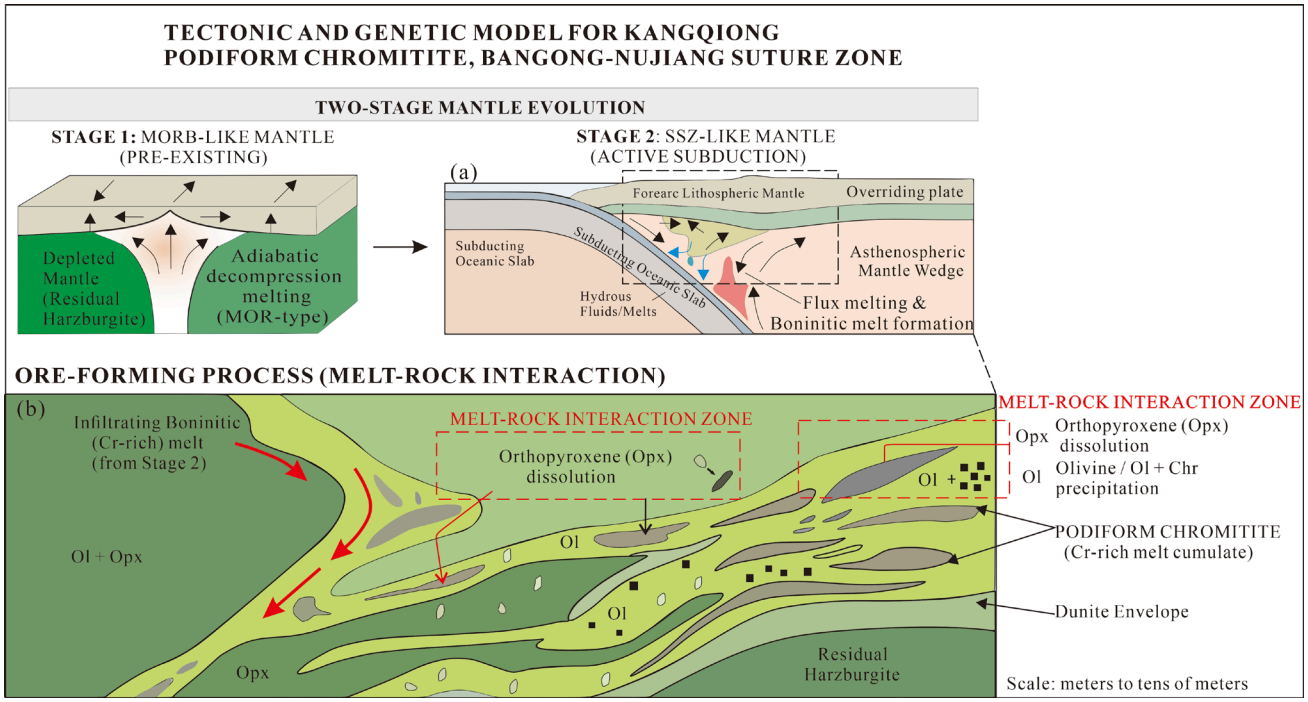



**Figure 7.** Tectonic and genetic model for the Kangqiong podiform chromitite in the Bangong-Nujiang Suture Zone. The two-stage mantle evolution driven by subduction initiation **(a)** is adapted from Zhang *et al.* (2024b). The schematic melt–rock interaction process **(b)**, illustrating orthopyroxene dissolution and the formation of a dunite envelope via melt-rock interaction is based on the models of Zhou *et al.* (1996) and González-Jiménez *et al.* (2014). Abbreviations: Ol, olivine; Opx, orthopyroxene; Chr, chromite; MOR, mid-ocean ridge; MORB, mid-ocean ridge basalt; mineral abbreviations follow Whitney and Evans (2010).

# 7. Conclusion

Based on the petrological, mineralogical, and geochemical investigations of the Kangqiong mantle peridotites and podiform chromitites, the main conclusions are as follows. The host peridotites show contrasting major-element compositions and depleted trace-element signatures, consistent with a heterogeneous history of melt extraction and compositional modification. Localized melt impregnation is one possible explanation for the Group A compositions, whereas the source and timing of fluid–rock modification remain uncertain.

The Kangqiong chromitites have $Cr^{\#}$ values of 65.06–66.58 and low $TiO_2$ contents. Together with the discrimination-diagram relationships and regional geological context, these features favour an SSZ-related interpretation and suggest a possible boninitic affinity of the parental melts. Melt–rock interaction provides a plausible mechanism for modifying melt composition and promoting chromian-spinel saturation and accumulation. A proposed two-stage model links an earlier episode of mantle melt extraction and localized modification to subsequent SSZ-related magmatism and chromitite formation. The model integrates the host-rock and mineral-chemical observations within the regional tectonic framework; the timing of chromitite formation and the detailed reaction sequence remain unconstrained.

### Data availability statement

No supplementary or additional data were generated in this study.

### Declaration of generative AI and AI-assisted technologies

During the preparation of this manuscript, the authors used Grammarly only to improve language and readability in limited sections of the manuscript. The authors take full responsibility for the content of the manuscript.

### Acknowledgments

Funding: This research is supported by the Special Fund of the Deep Earth Probe and Mineral Resources Exploration–National Science and Technology Major Project of China (Nos. 2025ZD1006103 and 2025ZD1006208) and the Deep Earth Probe and Mineral Resources Exploration–National Science and Technology Major Project (No. 2024ZD1000100).

### Authors' contribution

Conceptualization, X.L. and M.W.; methodology, X.L. and J.Z.; software, X.L. and Y.Z.; validation, M.W., Q.D. and J.Z.; formal analysis, X.L.; investigation, X.L., Z.L. and B.H.; resources, X.L.; data curation, X.L., Y.Z., and B.H.; writing—original draft preparation, X.L.; writing—review and editing, X.L., M.W., X.R.; visualization, X.L.; supervision, M.W.; project administration, M.W.; funding acquisition, M.W. All authors have read and agreed to the published version of the manuscript.

### Conflicts of interest

The authors declare no conflicts of interest.

## References


Arai S. Characterization of spinel peridotites by olivine-spinel compositional relationships: review and interpretation. *Chem. Geol.* 1994, 113(3–4):191–204. DOI: 10.1016/0009-2541(94)90066-3

Arai S. Control of wall-rock composition on the formation of podiform chromitites as a result of magma/peridotite interaction. *Resour. Geol.* 1997, 47(4):177–187. DOI: 10.11456/shigenchishitsu1992.47.177

Arai S, Miura M. Formation and modification of chromitites in the mantle. *Lithos* 2016, 264:277–295. DOI: 10.1016/j.lithos.2016.08.039

Bai W, Robinson PT, Fang Q, Yang J, Yan B, *et al.* Platinum-group elements and base metal alloys in podiform chromitites of the Luobusa ophiolite, southern Tibet (In Chinese). *Acta Geosci. Sin.* 2004, 25(4):385–396. DOI: 10.3321/j.issn:1006-3021.2004.04.001

Boynton WV. Cosmochemistry of the rare earth elements: meteorite studies. In *Rare Earth Element Geochemistry*. Amsterdam: Elsevier, 1984. pp. 63–114.

Cao C, Yang J, Yang S, Dong Y, Chen X, *et al.* The feature and tectonic setting of Dongqiao podiform chromitite in the central segment of the Bangong Lake-Nujiang suture zone in Tibet (In Chinese). *Acta Petrol. Sin.* 2022, 38(11):3391–3410. DOI: 10.18654/1000-0569/2022.11.09

Deschamps F, Godard M, Guillot S, Hattori K. Geochemistry of subduction zone serpentinites: a review. *Lithos* 2013, 178:96–127. DOI:10.1016/j.lithos.2013.05.019

Dilek Y, Furnes H. Ophiolite genesis and global tectonics: Geochemical and tectonic fingerprinting of ancient oceanic lithosphere. *Geol. Soc. Am. Bull.* 2011, 123(3–4):387–411. DOI: 10.1130/B30446.1

Droop GTR. A general equation for estimating $Fe^{3+}$ concentrations in ferromagnesian silicates and oxides from microprobe analyses, using stoichiometric criteria. *Mineral. Mag.* 1987, 51(361):431–435. DOI: 10.1180/minmag.1987.051.361.10

Fan S, Shi R, Ding L, Liu D, Huang Q, *et al.* Geochemical characteristics and zircon U-Pb age of the plagiogranite in Gaize ophiolite of central Tibet and their tectonic significance (In Chinese). *Acta Petrol. Mineral.* 2010, 29(5):467–478.

González-Jiménez JM, Griffin WL, Proenza JA, Gervilla F, O'Reilly SY, *et al.* Chromitites in ophiolites: how, where, when, why? Part II. The crystallization of chromitites. *Lithos* 2014, 189:140–158. DOI: 10.1016/j.lithos.2013.09.008

Hu P, Qiu T, Gong X, Xie H, Xu X, *et al.* Characteristics of the Gyaca chromite deposit in the eastern segment of the Yarlung–Zangbo suture zone in Xizang, China and their geological significances (In Chinese). *Bull. Mineral. Petrol. Geochem.* 2026, 45(2):376–390. DOI: 10.3724/j.issn.1007-2802.20260010

Leblanc M, Nicolas A. Ophiolitic chromitites. *Int. Geol. Rev.* 1992, 34(7):653–686. DOI: 10.1080/00206819209465629

Li G, Liu F, Zhu X, Liu P, Yang J. Characteristics of mineral chemistry and inclusions in high-chromium type and high-aluminum type chromitites from the Dingqing ophiolite in Tibet and their critical implication for tectonic setting (In Chinese). *Acta Petrol. Sin.* 2024, 40(12):3753–3780. DOI: 10.18654/1000-0569/2024.12.04

Li G, Yang J, Bo R, Rui H, Xiong F, *et al.* Dingqing ophiolite chromite in the eastern segment of Bangong Co-Nujiang suture zone, Tibet: occurrence characteristics and classifications (In Chinese). *Geol. China* 2019, 46(1):1–20. DOI: 10.12029/gc20190101

Li J, Zhai Q, Wang W, Tang Y, Hu P, *et al.* Subduction to closure of the Bangong–Nujiang Meso-Tethyan Ocean: constraints from Mesozoic magmatic rocks in the Jiang Co area, north-central Tibetan Plateau. *Geol. Soc. Am. Bull.* 2026, 138(1–2):215–231. DOI: 10.1130/B38155.1

Li S, Ding L, Guilmette C, Fu J, Xu Q, *et al.* The subduction-accretion history of the Bangong-Nujiang Ocean: constraints from provenance and geochronology of the Mesozoic strata near Gaize, central Tibet. Tectonophysics 2017, 702:42–60. DOI: 10.1016/j.tecto.2017.02.023

Li X, Li C, Wang M. Discovery of chromite in the Kangqiong area, central-western Bangong-Nujiang suture zone, Northern Tibet (In Chinese). *Geol. Bull. China* 2014, 33(11):1815–1819.

Lian D, Cai P, Rui H, Ma H, Cao S, *et al.* Discovery of chromitite orebody in the Cubuzha ophiolite of the western segment of the Yarlung–Zangbo ophiolitic belt, Xizang, China (In Chinese). *Acta Geol. Sin.* 2026, 100(3):1139–1142. DOI: 10.19762/j.cnki.dizhixuebao.2026035

Liu F, Yang J, Lian D, Li G. Geological features of Neothyan ophiolites in Tibetan Plateau and its tectonic evolution (In Chinese). *Acta Petrol. Sin.* 2020, 36(10):2913–2945. DOI: 10.18654/1000-0569/2020.10.01

Liu X, Zeng M, Li C, Chen S, Li T. Source and migration of fluids in a Meso-Tethyan subduction zone: fluid inclusion study of syn-mélange veins from the Mugagangri accretionary complex. *Minerals* 2023, 13(9):1196. DOI: 10.3390/min13091196

Liu Y, Zhai Q, Weinberg RF, Li S, Tang Y, *et al.* Identification of two-stage northward subduction of the Bangong-Nujiang Meso-Tethys Ocean, Tibetan Plateau. *Geol. Soc. Am. Bull.* 2026, 138(3–4):1259–1277. DOI: 10.1130/B38405.1

Ma H, Yang J. Tectonic setting of the Yarlung-Zangbo ophiolites: the perspective of podiform chromitite (In Chinese). *Acta Petrol. Sin.* 2025, 41(11):3735–3756. DOI: 10.18654/1000-0569/2025.11.07

Miladinova I, Kurz W, Hilmbauer-Hofmarcher T. Fluid-mantle interaction along the Mariana convergent margin. Geochem. Geophys. *Geosyst* 2023, 24(9):e2023GC010968. DOI: 10.1029/2023GC010968

Pearce JA, Barker PF, Edwards SJ, Parkinson IJ, Leat PT. Geochemistry and tectonic significance of peridotites from the South Sandwich arc-basin system, South Atlantic. *Contrib. Mineral. Petrol.* 2000, 139(1):36–53. DOI: 10.1007/s004100050572

Shi R, Cui G, Huang Q, Huang X, Zou H, *et al.* Diffusion-induced lithium isotopic heterogeneity in olivines from peridotites of an oceanized mantle lithosphere at the Yunzhug ophiolite (central Tibet). *Sci. Rep.* 2024, 14:4041. DOI: 10.1038/s41598-024-54616-6

Sun S, McDonough WF. Chemical and isotopic systematics of oceanic basalts: implications for mantle composition and processes. *Geol. Soc. Lond. Spec. Publ.* 1989, 42(1):313–345. DOI: 10.1144/GSL.SP.1989.042.01.19

Tang Y, Zhai QG, Hu PY, Liu YM, Wang W, *et al.* Genesis of mantle peridotites and high-Cr chromitites from the Jiangco ophiolite, northern Tibetan Plateau: Insights from mineralogy, geochronology, and geochemistry. *Ore Geol. Rev.* 2026, 191:107213. DOI: 10.1016/j.oregeorev.2026.107213

Wafik A, Ben Massoude M, Atif Y, Ait Lamqadem A, Rooki R, *et al.* Petrogenesis of serpentinites and chromitites in the Neoproterozoic Bou Azzer Ophiolite, Morocco: from mantle depletion to high-pressure exhumation. *Minerals* 2026, 16(5):460. DOI: 10.3390/min16050460

Wang Z, Yan J, Tang H, Xiao Y, Deng Z, *et al.* Geochemistry and mineralogy of peridotites and chromitites from Zhaheba Ophiolite Complex, Eastern Junggar, NW China: implications for the tectonic environment and genesis. *Minerals* 2023, 13(8):1074. DOI: 10.3390/min13081074

Wang B, Wang L, Chung S, Chen J, Yin F, *et al.* Evolution of the Bangong-Nujiang Tethyan ocean: insights from the geochronology and geochemistry of mafic rocks within ophiolites. *Lithos* 2016, 245:18–33. DOI: 10.1016/j.lithos.2015.07.016

Wang X, Bao P, Deng W, Wang F. *Xizang (Tibet) Ophiolites* (In Chinese). Beijing: Geological Publishing House, 1987.

Whitney DL, Evans BW. Abbreviations for names of rock-forming minerals. *Am. Mineral.* 2010, 95(1):185–187. DOI: 10.2138/am.2010.3371

Xie H, Gong X, He L, Mu X, Xu X, *et al.* Discussion regarding the characteristic comparison of ophiolites within the Bangongco-Nujiang suture zone and the prospects for chromite deposits (In Chinese). *Acta Geol. Sin.* 2025, 99(11):3664–3686. DOI: 10.19762/j.cnki.dizhixuebao.2025071

Xie H, Gui W, Gong X, He L, Qiu T, *et al.* Characteristics and genetic models of major chromitite deposit types worldwide (In Chinese). *Bull. Mineral. Petrol. Geochem.* 2026, 45(2):400–426. DOI: 10.3724/j.issn.1007-2802.20260004

Xiong F, Gong X, Qiu T, Xu X, Gui W, *et al.* Discussion on genesis of different types of minerals in the podiform chromitite deposit and constraint on the metallogenic process of the deposit (In Chinese). *Bull. Mineral. Petrol. Geochem.* 2025, 44(5):992–1007. DOI: 10.3724/j.issn.1007-2802.20240177

Xiong F, Xu X, Yang S, Yan J, Zhang B, *et al.* Genesis and significance of different types of mineral inclusions in podiform chromitite (In Chinese). *Acta Petrol. Mineral.* 2022, 41(2):413–436. DOI: 10.3969/j.issn.1000-6524.2022.02.013

Xiong Q, Zheng P, Dai H, Zhou X, Chen M, *et al.* The control of natures and processes of mantle on the ophiolite-type chromite mineralization (In Chinese). *Bull. Mineral. Petrol. Geochem.* 2026, 45(2):278–292. DOI: 10.3724/j.issn.1007-2802.20260009

Xu W, Li C, Xu M, Wu Y, Fan J, *et al.* Petrology, geochemistry, and geochronology of boninitic dikes from the Kangqiong ophiolite: Implications for the Early Cretaceous evolution of Bangong-Nujiang Neo-Tethys Ocean in Tibet. *Int. Geol. Rev.* 2015, 57(16):2028–2043. DOI: 10.1080/00206814.2015.1050464

Yang J, Lian D, Wu W, Yang Y, Cai P, *et al.* Chromitites in ophiolites: questions and thoughts (In Chinese). *Acta Geol. Sin.* 2022a, 96(5):1608–1634. DOI: 10.19762/j.cnki.dizhixuebao.2022226

Yang S, Li Y, Yang J, Ba D, Bo R, *et al.* Genesis and tectonic implications of podiform chromitite from the Renbu ophiolite in central Yarlung Zangbo suture zone, Tibet (In Chinese). *Acta Geol. Sin.* 2022b, 96(2):533–553. DOI: 10.19762/j.cnki.dizhixuebao.2022121

Yuan J, Zhang W, Pang Z, Li G, Chen G, *et al.* The characteristics of global podiform chromites and prospecting potential in China (In Chinese). *Earth Sci. Front.* 2025, 32(6):473–496. DOI: 10.13745/j.esf.sf.2025.5.32

Zeng Y, Xu J, Chen J, Wang B, Huang F, *et al.* Early Cretaceous (~138–134 Ma) forearc ophiolite and tectonomagmatic patterns in central Tibet: subduction termination and re-initiation of Meso-Tethys Ocean caused by collision of an oceanic plateau at the continental margin? *Tectonics* 2021, 40(3):e2020TC006423. DOI: 10.1029/2020TC006423

Zhang B, Xiong F, Xu X, Qiu T, Zhang C, *et al.* Geochemical characteristics and tectonic significance of Dongqiao podiform chromite in the middle segment of the Bangong-Nujiang suture zone (Tibet) (In Chinese). *Acta Geol. Sin.* 2024a, 98(11):3368–3392. DOI: 10.19762/j.cnki.dizhixuebao.2023198

Zhang P, Zhou M, Robinson PT, Malpas J, Yumul GP Jr, *et al.* Diversities of chromite mineralization induced by chemo-thermal evolution of the mantle during subduction initiation. *Nat. Commun.* 2024b, 15:9385. DOI: 10.1038/s41467-024-53508-7

Zhang QZ, Ba DZ, Xiong FH, Yang JS. Discussion on genesis process and deep prospecting breakthrough of Luobusa chromitite, Tibet (In Chinese). *Geol. China* 2017, 44(2):224–241. DOI: 10.12029/gc20170202

Zhou M, Robinson PT, Bai W. Formation of podiform chromitites by melt/rock interaction in the upper mantle. *Miner. Deposita* 1994, 29(1):98–101. DOI: 10.1007/BF03326400

Zhou MF, Robinson PT, Malpas J, Li Z. Podiform chromitites in the Luobusa ophiolite (Southern Tibet): implications for melt-rock interaction and chromite segregation in the upper mantle. *J. Petrol.* 1996, 37(1):3–21. DOI: 10.1093/petrology/37.1.3

Zhou M, Robinson PT, Su B, Gao J, Li J, *et al.* Compositions of chromite, associated minerals, and parental magmas of podiform chromite deposits: The role of slab contamination of asthenospheric melts in suprasubduction zone environments. *Gondwana Res.* 2014, 26(1):262–283. DOI: 10.1016/j.gr.2013.12.011

Zhu X, Liu F, Li Q, Liu P, Li G, *et al.* Information on continental lithospheric mantle in ophiolites: Geochemical evidence from mantle peridotites and chromitites of the Dingqing ophiolite, Tibet (In Chinese). *Acta Petrol. Sin.* 2025, 41(11):3757–3772. DOI: 10.18654/1000-0569/2025.11.08